processes

Article

A Novel SLOPDM Solar Maximum Power Point Tracking Control Strategy for the Solar Photovoltaic Power System

Hwa-Dong Liu [1], Shoeb-Azam Farooqui [2], Shiue-Der Lu [3], Yu-Lin Lee [2] and Chang-Hua Lin [2,*]

[1] Undergraduate Program of Vehicle and Energy Engineering, National Taiwan Normal University, Taipei 106, Taiwan; hdliu@ntnu.edu.tw
[2] Department of Electrical Engineering, National Taiwan University of Science and Technology, Taipei 106, Taiwan; m10907817@mail.ntust.edu.tw (S.-A.F.); d10807005@mail.ntust.edu.tw (Y.-L.L.)
[3] Department of Electrical Engineering, National Chin-Yi University of Technology, Taichung 411, Taiwan; sdl@ncut.edu.tw
* Correspondence: link@mail.ntust.edu.tw; Tel.: +886-2-2730-3289

Abstract: This study proposes a novel maximum power point tracking (MPPT) control strategy for the solar photovoltaic power system (SPPS). The proposed system adopts two solar photovoltaic modules of 430 W, which are connected to a boost converter and an MPPT controller, since the traditional MPPT algorithm (such as perturbation and observation [P&O] algorithm) can hardly reach maximum power point (MPP) under low irradiance level and partial shading conditions (PSC), which leads to the low efficiency of the SPPS. The speed of light optical path difference measurement (SLOPDM) MPPT control strategy has been developed in this study to overcome this problem. The estimation of the optical path angle difference is used as the basis for the proposed control strategy. This is done by determining the relationship between the optical path angle difference, solar photovoltaic power impedance R_{spv} and load R_o, and then calculating the duty cycle corresponding to the MPP, which then drives the boost converter to capture the MPP. The experimental results verify the proposed system, which shows the efficiency comparison between the SLOPDM MPPT algorithm, solar angle and horizon (SAH) algorithm, and P&O algorithm under PSC and uniform irradiance conditions (UIC) at irradiance levels of 700 W/m^2 and 65 W/m^2. It is evident from the comparison that the efficiency of the SLOPDM MPPT algorithm is 99% under both conditions, which is higher than the SAH and P&O algorithms. The SLOPDM MPPT algorithm can precisely, rapidly, and stably be operated at MPP. The contribution of this study is that the proposed MPPT control strategy can help achieve the high−performance of SPPS without changing the hardware circuit design and requiring any additional solar power meter. This reduces the cost and the complexity of the system significantly.

Keywords: maximum power point tracking; partial shading condition; perturbation and observation; speed of light optical path difference measurement; solar angle and horizon; solar photovoltaic module; solar photovoltaic power system; boost converter

Citation: Liu, H.-D.; Farooqui, S.-A.; Lu, S.-D.; Lee, Y.-L.; Lin, C.-H. A Novel SLOPDM Solar Maximum Power Point Tracking Control Strategy for the Solar Photovoltaic Power System. *Processes* **2022**, *10*, 1452. https://doi.org/10.3390/pr10081452

Academic Editor: Alfredo Iranzo

Received: 30 June 2022
Accepted: 23 July 2022
Published: 25 July 2022

1. Introduction

Due to the global climate change issue [1], every country is concerned with reducing carbon emissions and improving the greenhouse effect. First, the consumption of coal, natural gas, and other fossil fuels can be reduced significantly for power generation [2] to achieve this goal. Second, people should reduce the use of fossil fuels in transportation [3], and walking or riding bicycles can be preferred for shorter distances instead of driving. Furthermore, the government has already been promoting the utilization of renewable energy, such as wind power [4], solar power [5], hydroelectric power [6], tidal power [7], geothermal power [8], and biomass power [9], etc. Renewable energy is connected in parallel with the mains through power conversion technology and provides power to the demand side, as shown in Figure 1. Electricity is supplied to the demand side, which includes residential buildings, industries, campuses, commercial applications, rail vehicles [10], electric vehicles [11], etc. It is obvious from the aforesaid uses that renewable energy has been integrated into people's lives and has a wide range of applications.

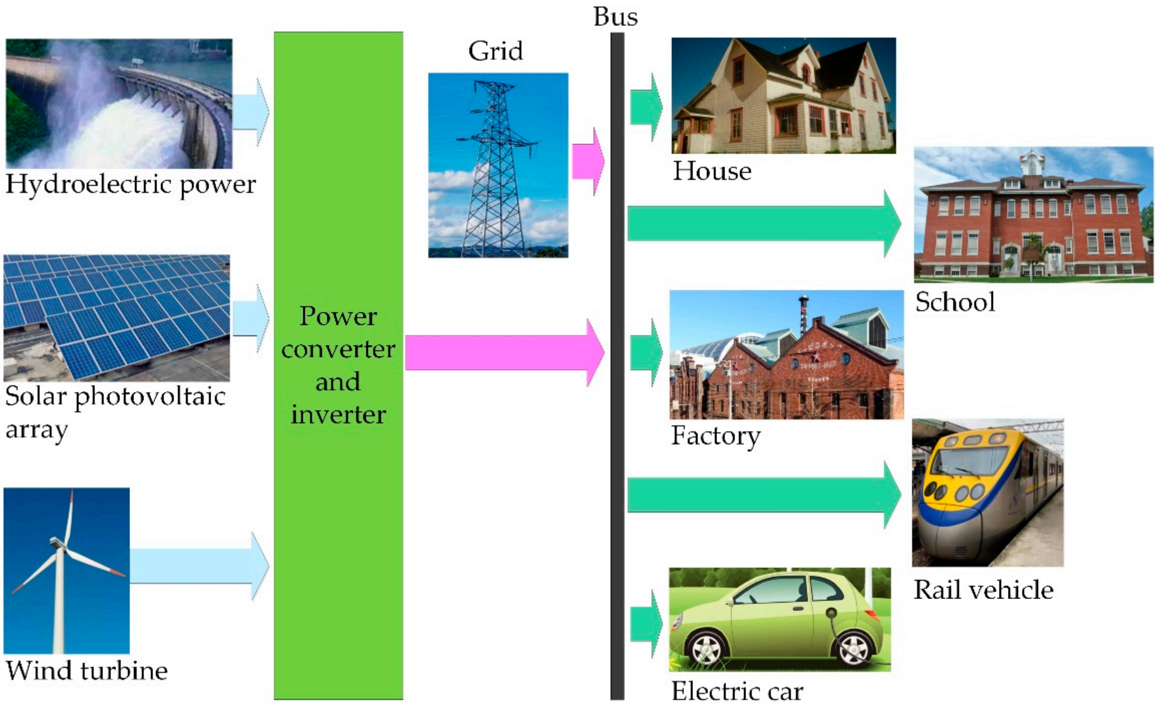

Figure 1. The schematic diagram of the grid with the renewable energy and the load demand.

Amongst the various renewable energy, the solar photovoltaic power system (SPPS) has drawn major attention of the researchers because SPPS does not generate noise during power generation and has a long service life [12]. The small solar photovoltaic module (SPVM) can be carried around conveniently and used in watches, computers, backpacks, blankets, etc. [13], which are more flexible in real life. Medium-sized solar photovoltaic arrays can be installed on rooftops to provide electricity for homes or farms [14]. A large-scale solar photovoltaic array parallel grid can improve users' stable power quality [15].

The SPPS is a diverse field and could have different research areas, including SPPS fault diagnosis [16], solar cell material upgrade [17], SPPS microgrid technology [18], and power electronics technology combined with the solar maximum power point tracking (MPPT) [19], etc. This study focuses on improving the efficiency of SPPS by developing a new MPPT technique that can help achieve higher efficiency under both uniform irradiance conditions (UIC) and partial shading conditions (PSC). Numerous studies focusing on MPPT have been presented. Kumar et al. discussed that the perturbation and observation (P&O) algorithm architecture is simple, easy to implement, and widely used in SPPS. However, the P&O algorithm uses the perturbation characteristic to track the maximum power point (MPP), which causes a power loss during the MPPT process. Additionally, the MPP cannot be achieved under PSC, resulting in low system performance [20]. Liu et al. examined the solar angle and horizon (SAH) algorithm to improve the performance of the hill−climbing algorithm. This SAH algorithm analyzes the solar angle and horizon with high efficiency under the UIC, but the efficiency decreases with environmental changes (as PSC) [21]. Lu et al. used the solar photovoltaic module output power and load (SPMOPL) MPPT control method to capture the MPP effectively. However, this SPMOPL MPPT control method needs huge data analysis (such as irradiance level, temperature, SPVM output voltage, etc.), which will cause a system burden [22]. Jagadeesan et al. proposed the right half−plane (RHP) MPPT control mechanism for tracking the MPP on the $P_{spv}-V_{spv}$ curve of SPVM to improve the system efficiency. This control mechanism reduces the MPPT range and thus reducing the system burden. However, the system efficiency will be low if the irradiance level and temperature change are high [23]. Uno et al. discussed the dual MPPT control strategy, which analyzed the SPVM and power converter output voltage and current signals to estimate the best duty cycle and capturing MPP. The dual MPPT control strategy has high efficiency but requires multiple power MOSFETs and diodes, which increases the system cost [24]. Mobarak et al. introduced the parabolic MPPT control strategy, which can make calculations quickly and accurately to improve SPPS efficiency. However, this control strategy must estimate multiple peak power points with the parabolic equations many times under the PSC and track the MPP. This will increase the system burden and the MPPT time [25]. Zhu et al. discussed the finite−state−machine (FSM) MPPT that can improve the system efficiency under the UIC and PSC. However, the complicated control sequence increases the burden on the controller. Also, the system requires multiple power converters to be used in parallel, which increases the cost of the system [26]. Kiran et al. introduced the variable step size artificial neural network (VSSANN) MPPT method that captures MPP through artificial intelligence training to improve system efficiency. However, the system requires the installation of an additional solar power meter and a thermometer, which makes the system costly [27].

This study proposes a speed of light optical path difference measurement (SLOPDM) MPPT based on estimating optical path difference angle. The proposed method calculates the duty cycle for the boost converter to track the MPP by using the relationship between optical path difference angle, solar photovoltaic module impedance R_{spv}, and load R_o. The proposed SLOPDM control strategy helps achieve the high performance of the SPPS under both the UIC and PSC, verified by the experimental result. The proposed SLOPDM-based MPPT is fast, simple, low-cost, and does not cause a system burden.

Table 1 shows a comparison of various MPPT algorithms. The following points can be concluded from this table. First, the proposed SLOPDM algorithm is the least complex among the aforementioned algorithms. Second, the proposed algorithm performs better than the P&O and RHP MPPT algorithms. Last, the MPP tracking speed of the proposed algorithm is superior to the P&O, SAH, SPMOPL, dual MPPT, and FSM MPPT algorithms.

Table 1. Comparison of various MPPT algorithms.

Algorithm	Complexity	Performance	MPPT Speed
P&O algorithm [20]	Low	Medium	Low
SAH algorithm [21]	Medium	High	Medium
SPMOPL algorithm [22]	Medium	High	Medium
RHP MPPT algorithm [23]	Low	Medium	High
Dual MPPT algorithm [24]	Medium	High	Medium
Parabolic MPPT algorithm [25]	Medium	High	High
FSM MPPT algorithm [26]	High	High	Medium
VSSANN MPPT algorithm [27]	Medium	High	High
Proposed SLOPDM algorithm	Low	High	High

2. The Proposed Solar Photovoltaic Power System

2.1. The Configuration of the Solar Photovoltaic Module

A solar photovoltaic cell (SPVC) is composed of multiple P−N junction semiconductors, which convert light energy into electrical energy. Figure 2 displays the equivalent circuit of a single SPVC, where I_{ph} is the current produced by the SPVC, R_{pn} is the non−linear resistance of the P−N junctions, D_{pn} is the P−N junction diode, R_{sh} and R_s represent the equivalent parallel resistance and the series resistance of the SPVC, respectively, V_{spv} and I_{spv} represent the output voltage and current of the SPVC [28].

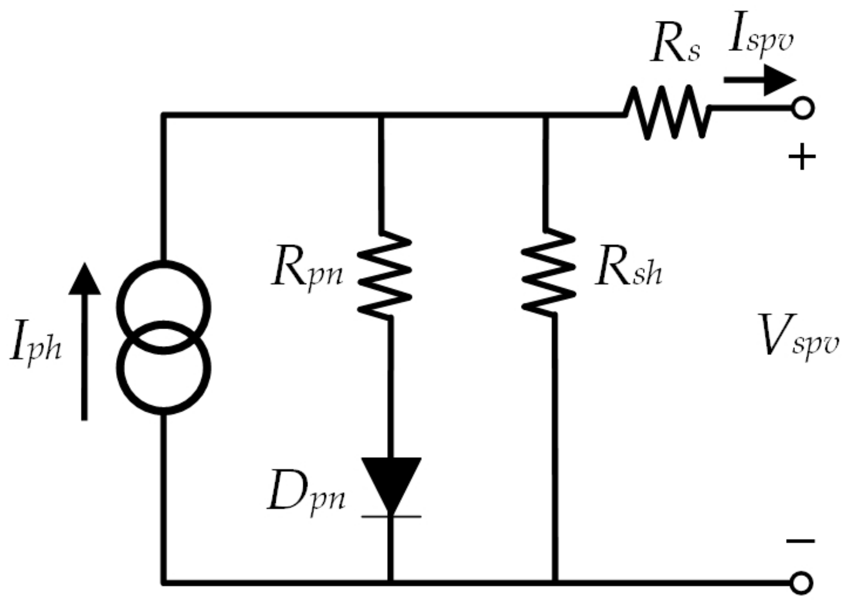

Figure 2. The equivalent circuit of a single SPVC.

The equivalent circuit of a single SPVC is shown in Figure 2. Using the P−N junction characteristic, the formula of its output current I_{spv} is expressed as follows:

$$I_{spv} = n_p I_{ph} - n_p I_r \left[\exp\left(\frac{qV_{spv}}{kTAn_s} \right) - 1 \right] \tag{1}$$

where n_p is the number of SPVC in parallel, n_s is the number of SPVC in series, q is the quantity of electric charge (1.6×10^{-19} C), k is the Boltzmann constant (1.38×10^{-23} J/°K), T is the temperature of SPVC, and A is SPVC's ideality factor.

In Equation (1), I_r represents the SPVC's reverse saturation current, which can be expressed as follows:

$$I_r = I_{rr} \left(\frac{T}{T_r} \right)^3 \exp\left[\frac{qE_{Gap}}{kA} \left(\frac{1}{T_r} - \frac{1}{T} \right) \right] \tag{2}$$

where T_r is the reference temperature of SPVC, I_{rr} is the reverse saturation current of SPVC at temperature T_r, and E_{Gap} is the energy across the band gap of semiconductor material.

Figure 3 displays the schematic diagram of the SPVC, solar photovoltaic module (SPVM), and solar photovoltaic array [29]. Solar photovoltaic cells can be connected in parallel and series to form an SPVM, whereas a solar photovoltaic array is composed of multiple SPVMs with series and parallel connections.

2.2. Solar Photovoltaic Module's Connection with Power Electronic Converter

This study adopts two SPVMs and implements the experiment with the solar photovoltaic simulator, where the specification of a single solar photovoltaic module is shown in Table 2. When the irradiance level (IL) = 1000 W/m^2 and the temperature = 25 °C, the single SPVM has an open−circuit voltage V_{oc} = 50 V, short−circuit current I_{sc} = 6 A, maximum power point voltage V_{MPP} = 40 V, maximum power point current I_{MPP} = 5.4 A, and maximum power point power P_{MPP} = 215 W.

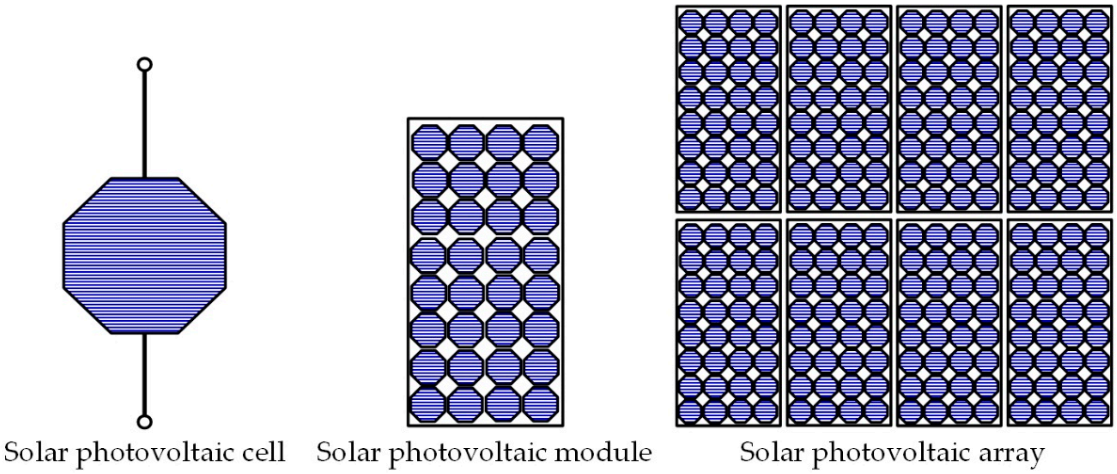

Figure 3. The schematic diagram of SPVC, SPVM, and a solar photovoltaic array.

Table 2. Specifications of a single SPVM.

Parameters	Value
V_{oc}	50 V
I_{sc}	6 A
V_{MPP}	40 V
I_{MPP}	5.4 A
P_{MPP}	215 W

In SPPS, the output voltage of SPVM is low. The power electronic converter can increase the voltage level up to a value required by the load and facilitate the stable voltage, so power electronics technology is widely used in SPPS. In addition, the MPPT controller can further enhance the SPVM output power (as shown in Figure 4) by sensing the output voltage or current of the SPVM. Accordingly, pulse−width modulation (PWM) signal is generated for the power switches which drive the converter. There are many kinds of power electronic converters employed in the MPPT controller for SPPS, such as single-ended primary inductor converter (SEPIC), buck-boost, Flyback, boost converters, etc. [30–33]. The boost converter [30] is most commonly used in MPPT systems mainly because of its merit of having a simple circuit structure, easy implementation, and high efficiency. Therefore, the boost converter has been selected as the power electronic converter in this study [30].

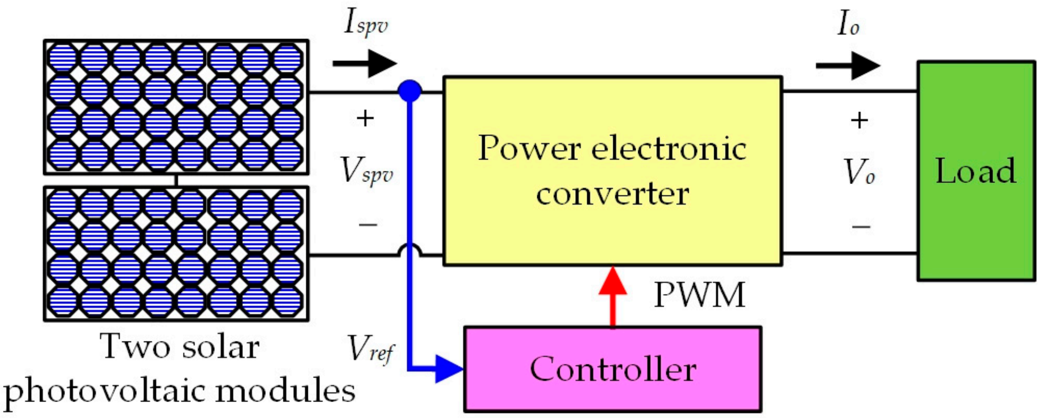

Figure 4. The schematic diagram of two SPVMs connected with a power electronic converter.

The relationship between output voltage V_o, SPVM voltage V_{spv}, and duty cycle D is shown as follows:

$$V_o = \frac{V_{spv}}{1-D} \tag{3}$$

The relationship between output current I_o, SPVM current I_{spv}, and duty cycle D is expressed as:

$$I_o = I_{spv}(1-D) \tag{4}$$

The relationship between the load impedance R_o, SPVM impedance R_{spv}, and duty cycle D is displayed as follows:

$$\frac{R_o}{R_{spv}} = \frac{1}{(1-D)^2} \tag{5}$$

where load impedance R_o = V_o/I_o and SPVM impedance R_{spv} = V_{spv}/I_{spv}.

Table 3 shows the SPVC efficiency range [34]. The material included monocrystalline silicon, polycrystalline silicon, amorphous silicon, monocrystalline compound, and polycrystalline compound with a conversion efficiency range of 15~2 %, 12~18%, 6~9%, 18~30%, and 10~12%, respectively. Different SPVC materials have different conversion efficiencies. Therefore, SPVM impedance and SPVM output power are also different.

Table 3. The SPVC efficiency range.

SPVC Material	Conversion Efficiency Range
Monocrystalline silicon	15~20%
Polycrystalline silicon	12~18%
Amorphous silicon (Sic, SiGe, and SiH)	6~9%
Monocrystalline compound (GaAs, InP)	18~30%
Polycrystalline compound (CdS, CdTe)	10~12%

When sunlight hits the SPVM connected to the load, it will generate V_{spv} and I_{spv}. However, the SPVM structure has a key effect on the SPVM impedance and the SPVM output power. An SPVM structure includes soda lime glass (SLG), ethylene vinyl acetate (EVA), SPVC, and back layer, etc. [34], as shown in Figure 5. If the SPVM structure is of poor quality, damaged, and has other abnormal problems, it will affect the SPVM output power. Although, many factors affect SPVM's output power. However, this study proposed an MPPT that can be used to achieve the best system performance for various types of SPVM.

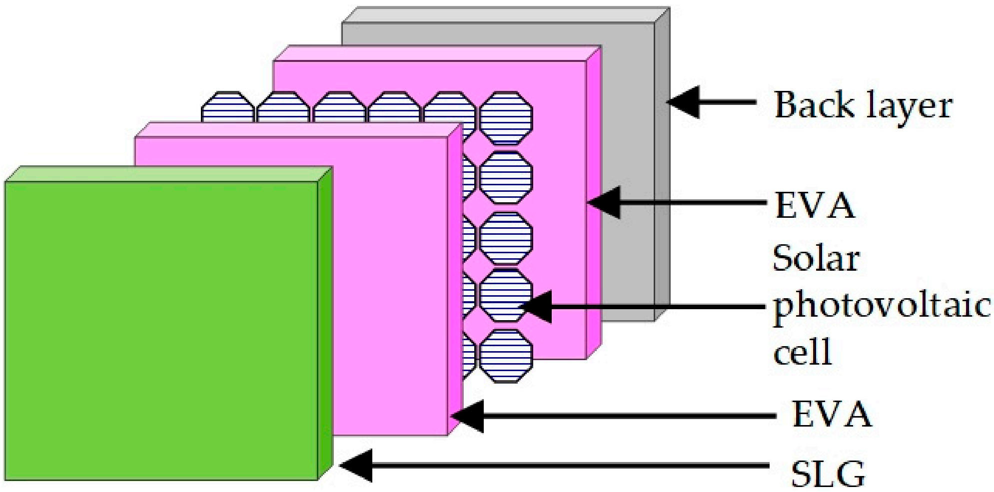

Figure 5. The schematic diagram of SPVM structure.

The system used in this study is structured as two SPVMs connected in series. The input of the boost converter is connected to SPVMs, whereas the output is connected to the load. Secondly, the MPPT control strategy is embedded in the controller (Figure 4). Finally, the controller generates the PWM signal for the boost converter to capture MPP depending on the proposed SLOPDM MPPT control strategy. The details about the proposed SLOPDM MPPT control strategy for the SPPS can be seen in Section 3.

3. Proposed Speed of Light Optical Path Difference Measurement MPPT Control Strategy

Figure 6 is the schematic diagram showing the relationship between the sun, earth, and planets, where the sunlight shines on the planet and the planet reflects the light to the earth. However, the earth revolves around the sun. It leads to the position of the planet seen on the earth being different from the actual position of the planet due to the speed combination of the earth's revolution and light. It is similar to being on a running train when it's raining outside, and the rain looks like it is falling diagonally when observed from inside the train car.

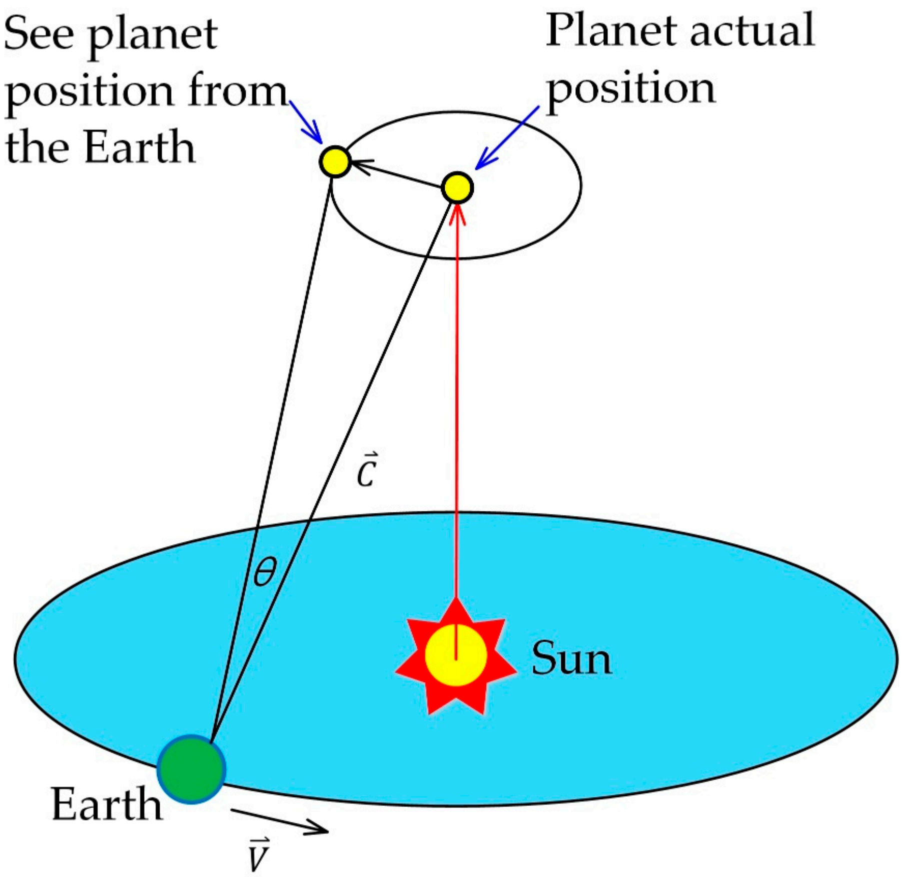

Figure 6. Relationship diagram of sun, earth, and planet.

In the 18th century, Prof. Bradley proposed the speed of light optical path difference measurement (SLOPDM) method to calculate the actual planetary position. The planetary position could be calculated accurately using this method [35]. This study extends the use of the SLOPDM method for maximum power point tracking. So, the proposed MPPT method in this study is named SLOPDM MPPT. A detailed description of the proposed MPPT control strategy has been presented below.

In Figure 6, the earth's revolution speed is $\vec{V}$, the speed of light reflected by the planet $\vec{C}$ is 3×10^5 km/s, and the angle of the optical path difference is θ. Figure 7 demonstrates a schematic diagram of the relationship between the earth's revolution speed $\vec{V}$, the light speed $\vec{C}$, and the angle of the optical path difference θ, which can also be represented by Equation (6).

$$\vec{C} = \frac{\vec{V}}{\tan\theta} \tag{6}$$

where $\vec{C}$ is constant as 3×10^5 km/s, $\vec{V}$ changes with the distance between the sun and the earth. $\vec{V}$ becomes higher when the distance between the earth and the sun is reduced. Therefore, $\vec{V}$ is not constant.

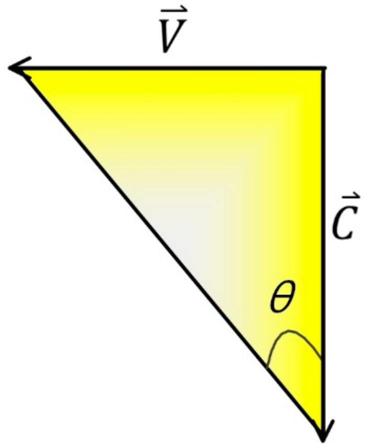

Figure 7. The schematic diagram of the relationship between $\vec{V}$, $\vec{C}$, and θ.

Figure 8 is transformed from Figure 7, which shows the relationship between angle θ_1 and its opposite Y. In Figure 8, the radius of the circle is regarded as 1 depending on the light speed $\vec{C}$, which is a constant value; angle θ_1 corresponds to the angle of the optical path difference θ. Using Equation (5), Figures 7 and 8 and assuming that Y is proportional to the $\vec{V}$ and R_{spv}, the relationship between $\vec{V}$, Y, R_{spv}, R_o, and duty cycle D are expressed as Equation (7).

$$\vec{V} \propto Y \propto R_{spv} = R_o(1 - D)^2 \tag{7}$$

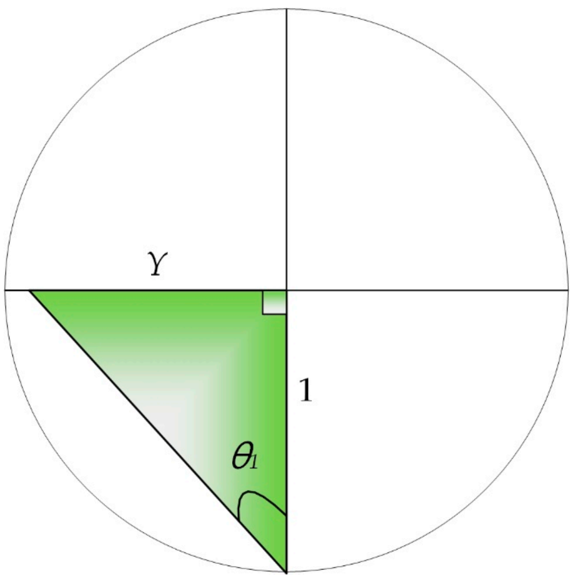

Figure 8. The relationship diagram of angle θ_1 and its opposite Y.

When $\theta_1 = 0°$, $\overrightarrow{C}$ is proportional to the radius (1). By substituting Equation (6) into (7), the relationship between tanθ_1, R_{spv}, R_o, and duty cycle D can be obtained as follows:

$$\begin{gathered}\tan\theta_1 \cdot \overrightarrow{C} = \overrightarrow{V} \propto D^2 - 2D + \left(1 - \frac{R_{spv}}{R_o}\right) = 0 \\ \tan\theta_1 \propto D^2 - 2D + \left(1 - \frac{R_{spv}}{R_o}\right) = 0\end{gathered} \tag{8}$$

When $\theta_1 = 45°$, Equation (8) will be transformed into Equation (9).

$$\begin{gathered}\tan\theta_1 \cdot \overrightarrow{C} = \overrightarrow{V} \propto D^2 - 2D + \left(1 - \frac{R_{spv}}{R_o}\right) = 1 \\ \tan\theta_1 \propto -D^2 + 2D + \frac{R_{spv}}{R_o} = 1\end{gathered} \tag{9}$$

If the value of R_{spv} and R_o are known, the duty cycle D at $\theta_1 = 0°$ and $\theta_1 = 45°$ can be calculated using Equations (8) and (9), respectively. Therefore, this study can estimate the MPPT's duty cycle to achieve MPP using the relationship between tanθ_1, R_{spv}, R_o, and duty cycle D.

Using the transformation of Equations (5)−(9), the relationship between R_{spv}, angle θ_1, and duty cycle D can be drawn, as shown in Figure 9. In Figure 9, the right $y-$axis represents the impedance of SPVMs R_{spv}; the left $y-$axis represents the duty cycle D; the $x-$axis represents the angle; the straight blue line shows the results when R_{spv} changes from 1 Ω to 46 Ω; and the brown curve shows the results when D changes from 0 to 0.1. When load R_o = 200 Ω, R_{spv} = 34 Ω, angle = 34° using the Equations (5)–(9), 0.06 is the optimal duty cycle of the MPPT, because the proposed SLOPDM MPPT control strategy regards the optical path difference measurement of the light speed as the basis and considers the relationship between the load R_o and R_{spv} to calculate the MPPT duty cycle D. Therefore, the proposed SLOPDM control strategy can capture the MPP rapidly and accurately.

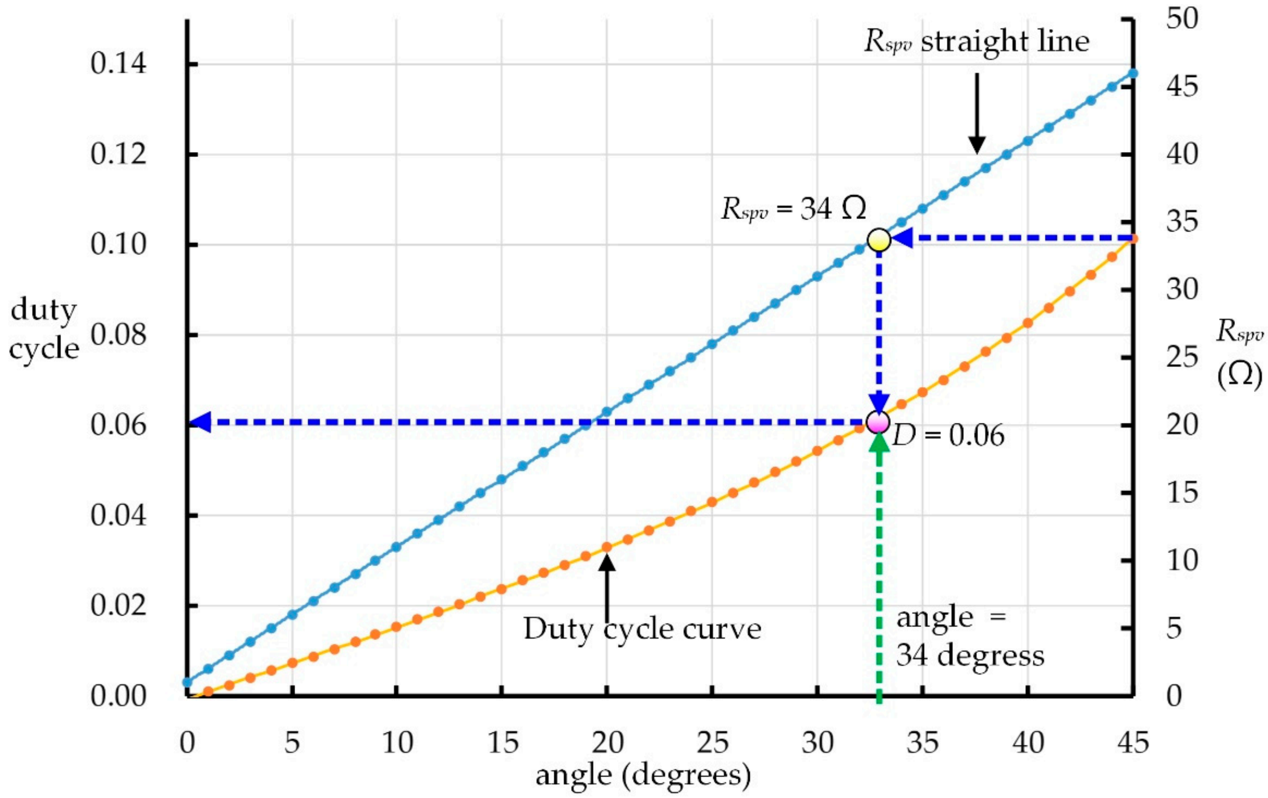

Figure 9. The relationship between R_{spv}, angle θ_1, and duty cycle D.

Figure 10 shows the flowchart of the proposed SLOPDM MPPT control strategy. First, the system measures V_{spv}, I_{spv}, V_o, and I_o. The R_{spv} and R_o will only be calculated when the boost converter's output current $I_o \neq 0$. Second, the dP_{spv}/dV_{spv} is the next parameter to be checked. If dP_{spv}/dV_{spv} = 0, the system is operating at MPP and the duty cycle D is fixed. By contrast, if $dP_{spv}/dV_{spv} \neq 0$, the proposed SLOPDM MPPT will be performed. Next, the system calculates the angel with R_{spv} and R_o (Figure 9). Finally, the system substitutes R_{spv}, R_o, and angle θ_1 into Equation (8) to obtain the MPPT's duty cycle D, and drives the boost converter to capture the MPP.

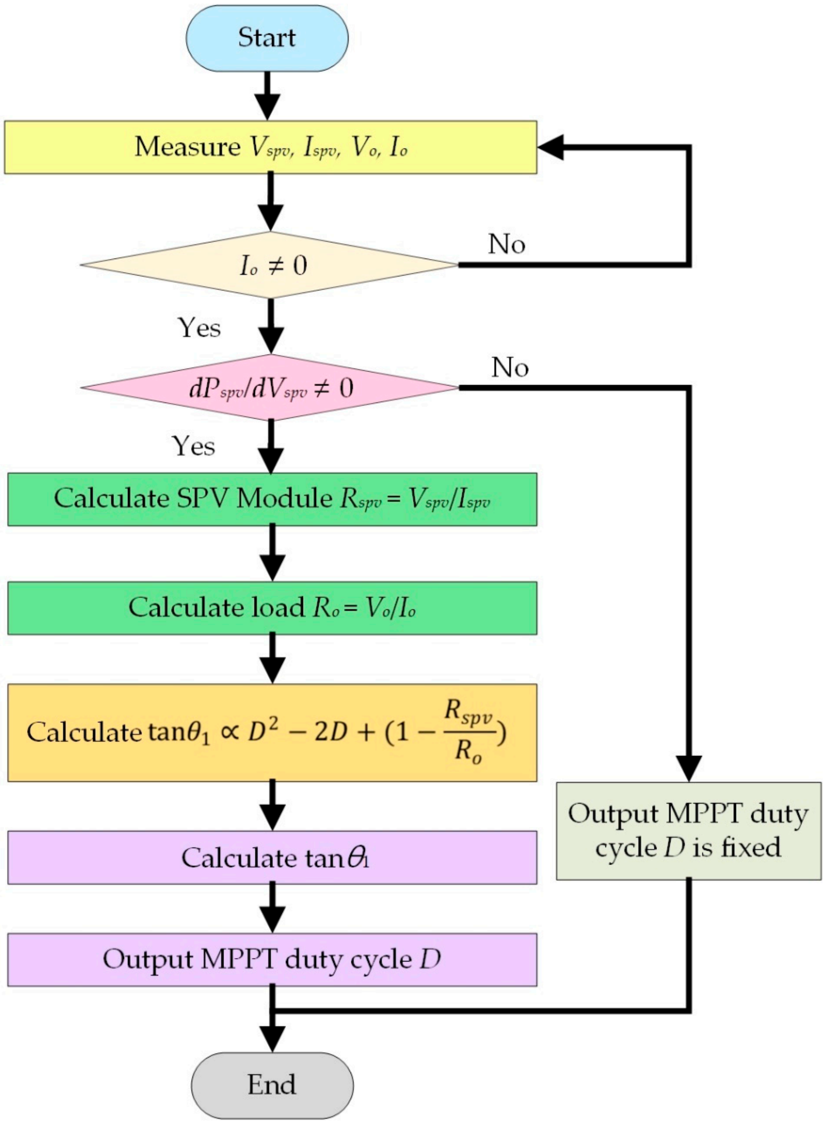

Figure 10. Flowchart of the proposed SLOPDM MPPT control strategy.

Figure 11 displays the architecture diagram of the solar photovoltaic simulator that connects the boost converter and embeds the proposed SLOPDM MPPT control strategy. The solar photovoltaic simulator simulates two SPVMs connected in series whose total rated power is 430 W, and the specification of a single SPVM is shown in Table 2. The specifications of the boost converter inductor L_1 and capacitor C_1, as well as the microcontroller unit (MCU), are shown in Table 4. The control flow of the proposed SLOPDM MPPT strategy is explained as follows: First, the voltage and current sensors are employed at the solar photovoltaic simulator's output V_{spv} and I_{spv} to capture the voltage $V_{spv,ref}$ and current $I_{spv,ref}$ signals to be transmitted to the MCU. Second, the boost converter's output V_o and I_o uses voltage and current sensors to catch the voltage $V_{o,ref,}$ and current $I_{o,ref}$ signals transmitted to the MCU. Third, the $V_{spv,ref}$, $I_{spv,ref}$, $V_{o,ref}$, and $I_{o,ref}$ signals are utilized to calculate the MPPT duty cycle using the proposed SLOPDM MPPT control strategy, whose operating frequency is 50 kHz. Finally, the MCU generates the MPPT duty cycle to drive the power MOSFET SW_1 of the boost converter, thus tracking the MPP.

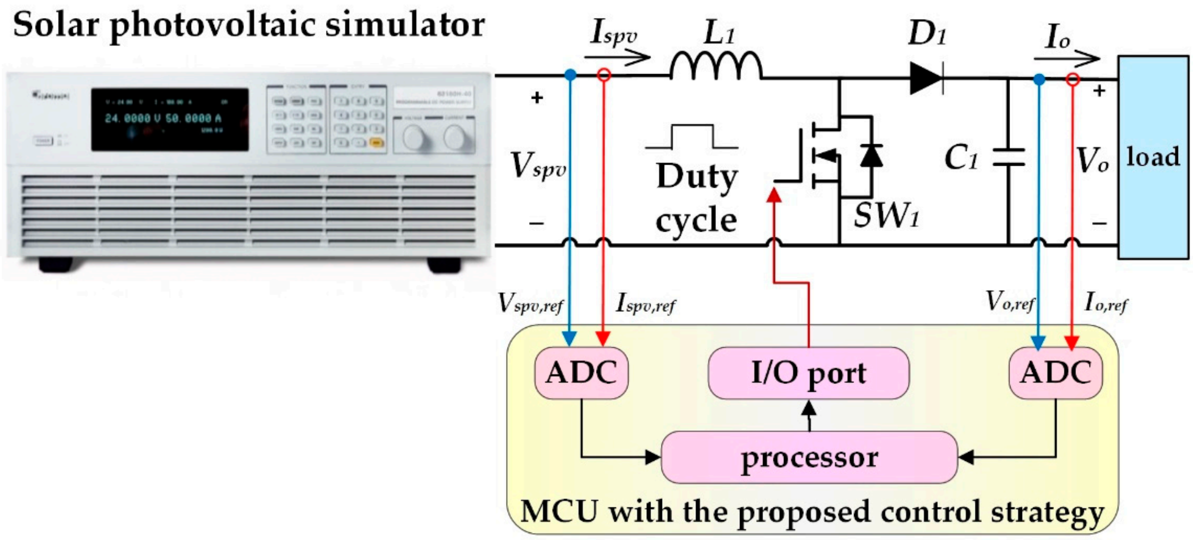

Figure 11. Architecture diagram of the solar photovoltaic simulator connected with the boost converter and embeds the proposed control strategy.

Table 4. The specification of the boost converter and the MCU.

Parameter	Specification
MCU	Microchip, model number: 18F4520
L_1 of the boost converter	0.5 mH
C_1 of the boost converter	330 µF

4. Experiment Results

The prototype of the solar photovoltaic system used in this study is displayed in Figure 12. The specification of this experimental setup is shown in Table 5. In this study, the proposed SLOPDM control strategy, SAH, and P&O algorithms have been experimentally implemented under both the UIC and PIC with the irradiance level (IL) of 700 W/m^2 and 65 W/m^2. A comparative analysis of these control strategies has also been performed to demonstrate the effectiveness of the proposed control strategy. The experiment results verify that the efficiency of the proposed SLOPDM algorithm is higher than that of the SAH and P&O algorithms.

Table 5. Specifications of the experimental setup.

Equipment/Components	Specification
Solar photovoltaic simulator	Chroma, model number: 62020H
Computer	ASUS, model number: X515E
Scope	Tektronix, model number: DPO 2014B
Power supply	Gwinstek, model number: GPS−4303Wanptek, model number: NPS306W
Load R_o	70 Ω and 450 Ω

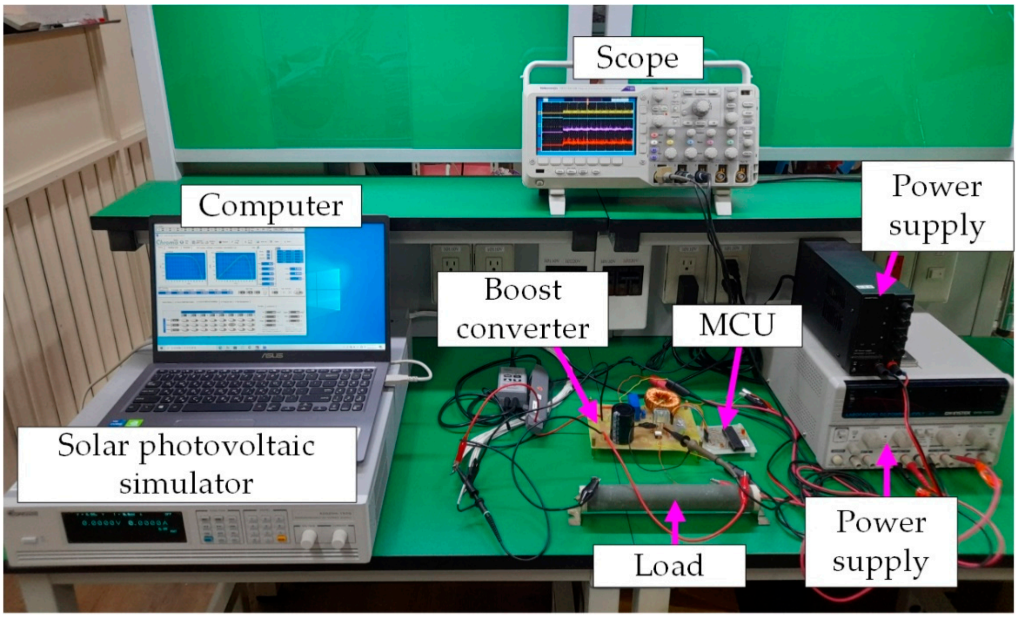

Figure 12. A prototype of the solar photovoltaic system.

4.1. Experimental Results under Uniform Irradiance Condition

Figure 13 displays the gate−source voltage of the power MOSFET (v_{gs}), output voltage (V_o), output current (I_o), and output power (P_o) waveforms of the boost converter under the test condition having IL = 700 W/m^2, the temperature = 25 °C obtained by implementing certain control strategies. Figure 14 shows the $P_{spv}-V_{spv}$ characteristic curve of the SPVM at IL = 700 W/m^2 and the temperature = 25 °C obtained using certain control strategies.

Figure 13a displays the experimental results of the proposed SLOPDM MPPT control strategy. Figure 13b,c are the results of the SAH and P&O algorithms, respectively. First, R_{spv} and R_o were calculated using V_{spv}, I_{spv}, V_o, and I_o measurements of 21.2 Ω and 70 Ω, respectively. Second, angle θ_1 and MPPT duty cycle D were estimated using Equation (8) and Figure 9, which are 1.4° and 0.43, respectively. The proposed SLOPDM control strategy produced the duty cycle D = 0.43, V_o = 140 V, and V_{MPP} = 80.6 V (from Equation (3)) for the SPPS and the actuating point accurately operate at MPP P_{mpp} = 305 W at t = t_a as demonstrated in Figure 14a. The SAH algorithm's actuating point operating at MPP P_{mpp} = 305 W is shown in Figure 14b, whereas the P&O algorithm's actuating point operating at MPP P_{mpp} = 305 W is depicted in Figure 14c.

Figure 15 demonstrates the waveforms of the gate−source voltage of the power MOSFET (v_{gs}), output voltage (V_o), output current (I_o), and output power (P_o) of the boost converter at IL = 65 W/m^2 and temperature = 25 °C by implementing certain control strategies. Figure 16 shows the $P_{spv}-V_{spv}$ characteristic curve of the SPVM at IL = 65 W/m^2 and temperature = 25 °C obtained using certain control strategies.

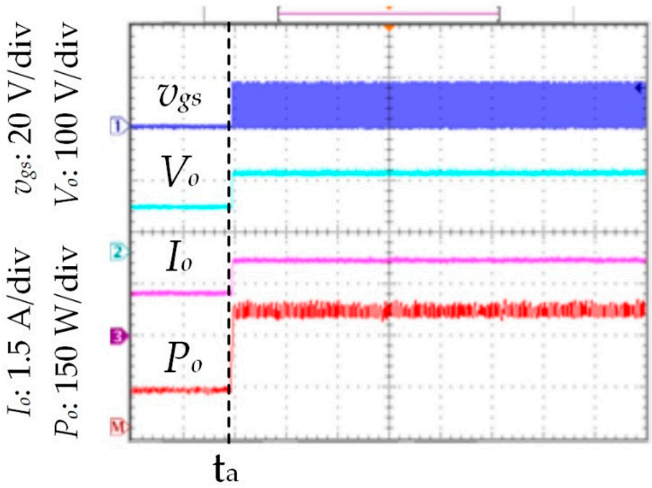

(**a**)

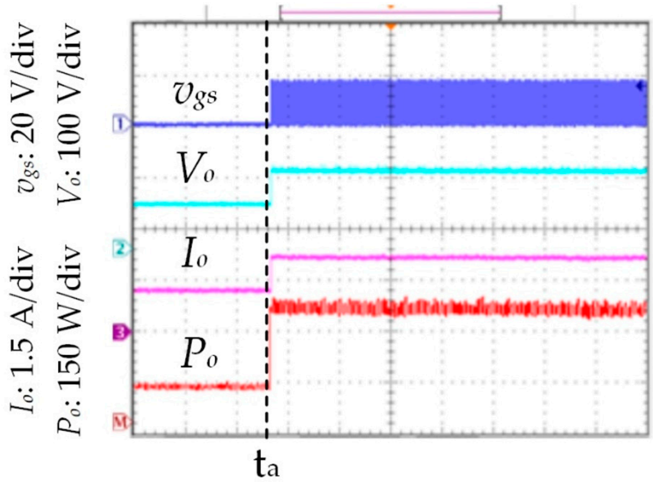

(**b**)

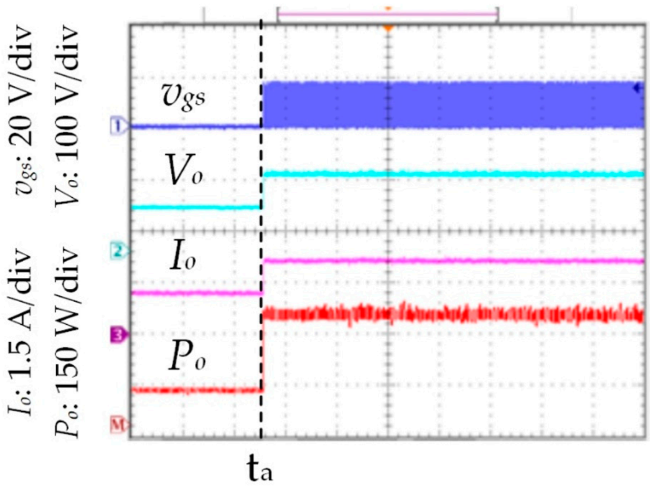

(**c**)

Figure 13. The waveforms of v_{gs}, V_o, I_o, and P_o under UIC with IL = 700 W/m^2 and temperature = 25 °C by implementing the control strategy (**a**) SLOPDM, (**b**) SAH, and (**c**) P&O algorithms. (Horizontal axis: 2 s/div).

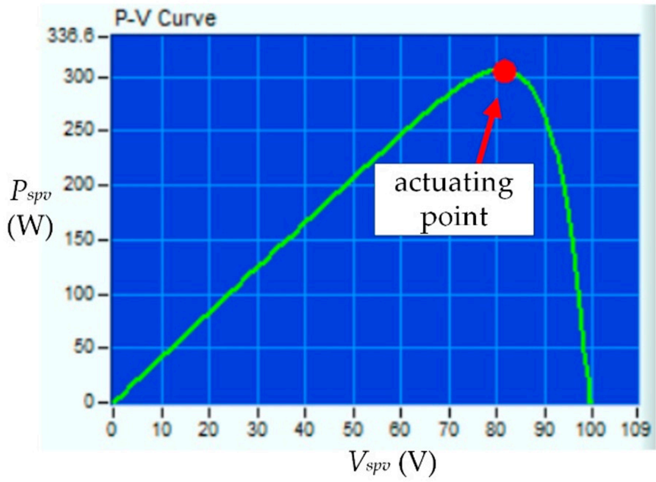

(**a**)

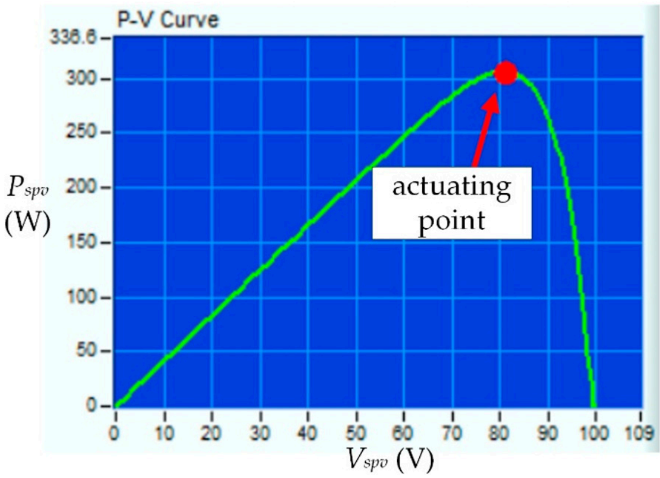

(**b**)

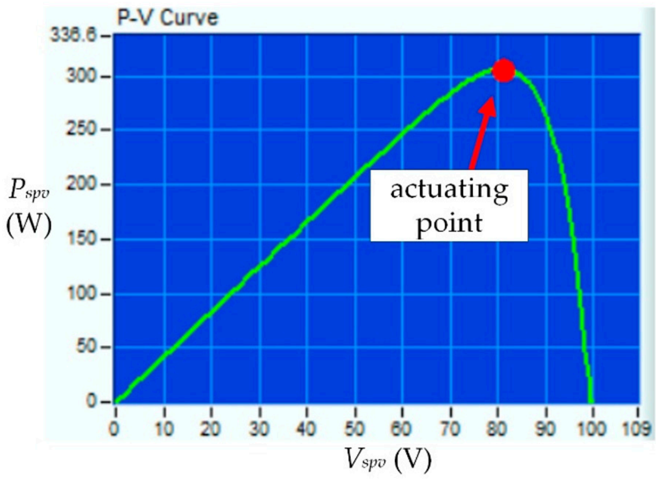

(**c**)

Figure 14. $P_{spv}-V_{spv}$ characteristic curve of SPVM under UIC at IL = 700 W/m^2 and temperature = 25 °C by using the control strategy (**a**) SLOPDM, (**b**) SAH, and (**c**) P&O algorithms.

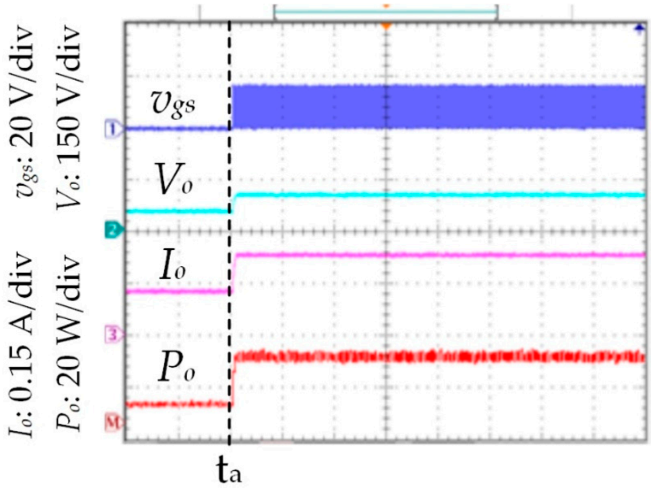

(**a**)

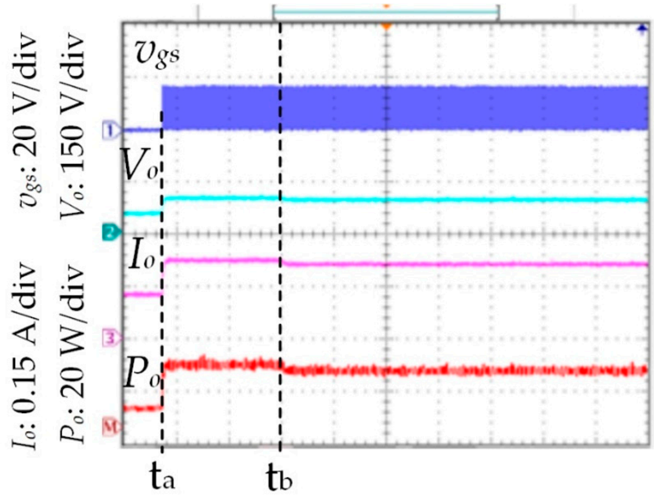

(**b**)

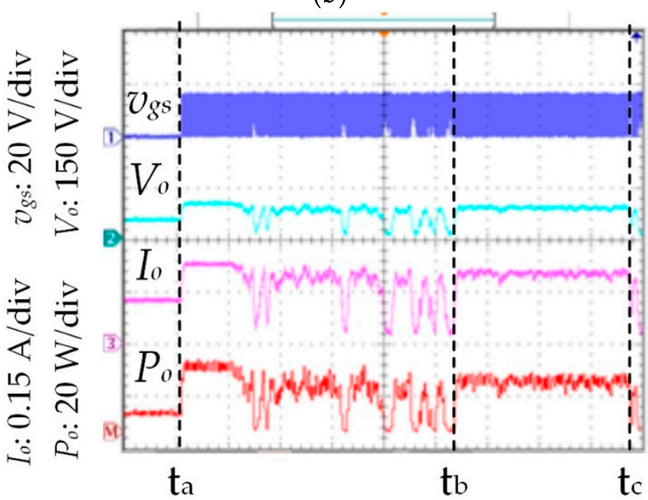

(**c**)

Figure 15. The waveforms of v_{gs}, V_o, I_o, and P_o under UIC at IL = 65 W/m^2 and temperature = 25 °C by implementing the control strategy (**a**) SLOPDM, (**b**) SAH, and (**c**) P&O algorithms. (Horizontal axis: 2 s/div).

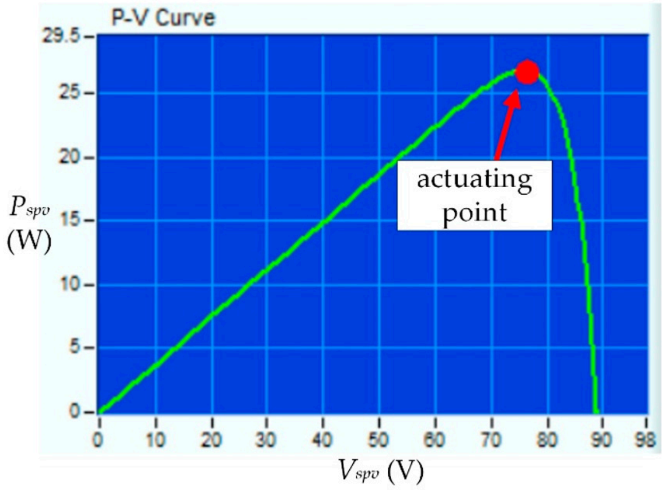

(**a**)

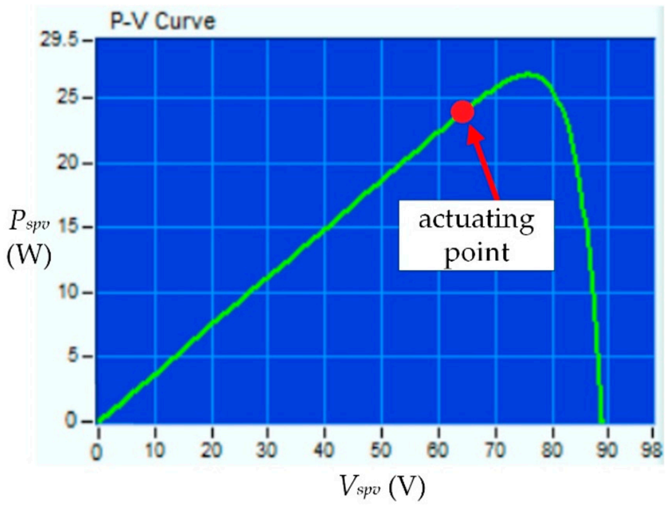

(**b**)

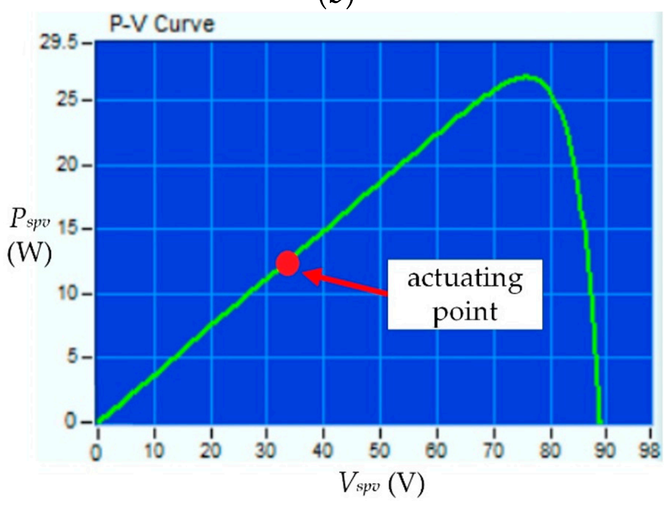

(**c**)

Figure 16. $P_{spv}-V_{spv}$ characteristic curve of SPVM under UIC at IL = 65 W/m^2 and temperature = 25 °C by using the control strategy (**a**) SLOPDM, (**b**) SAH, and (**c**) P&O algorithms.

Figure 15a displays the experimental results of the proposed SLOPDM MPPT control strategy. Figure 15b,c are the results of the SAH and P&O algorithms, respectively. First, R_{spv} and R_o were calculated using V_{spv}, I_{spv}, V_o, and I_o measurements of 213.8 Ω and 450 Ω, respectively. Second, angle θ_1 and MPPT duty cycle D were estimated using Equation (8) and Figure 9, which are 2.47° and 0.28, respectively. The proposed SLOPDM control strategy produced the duty cycle D = 0.28, V_o = 105 V, and V_{MPP} = 75.7 V (from Equation (3)) for the SPPS and the actuating point accurately operate at MPP P_{mpp} = 26.6 W at t = t_a as demonstrated in Figure 16a. The SAH algorithm's actuating point operates the same as the proposed method at MPP P_{mpp} = 26.6 W at t = t_a while the actuating point moves away from the MPP at t = t_b, and the power drops to P_{mpp} = 24.5 W, as shown in Figure 16b. This is because the SAH algorithm performs poorly under the low irradiance level condition (LILC). In Figure 16c, the P&O algorithm's actuating point operated unstably until t = t_b. When t = t_c, the actuating point becomes unstable again. The MPP captured by the P&O algorithm P_{mpp} is 12.5 W, as depicted in Figure 16c. The reason is that the P&O algorithm cannot efficiently track MPP with perturbation characteristics under the LILC.

The above results are organized in Table 6, which shows the comparison of proposed SLOPDM, SAH, and P&O algorithms under UIC. The proposed SLOPDM algorithm can reach 99% efficiency at the IL = 700 W/m^2 and 65 W/m^2, which is higher than the efficiency of SAH and P&O algorithms.

Table 6. The comparison of proposed SLOPDM, SAH, and P&O algorithms under UIC.

Algorithm	**Efficiency**	
	IL = 700 W/m^2	**IL = 65 W/m^2**
SAH	99%	91%
P&O	99%	47%
SLOPDM	99%	99%

4.2. Experimental Results under the Partial Shading Conditions

Figure 17a shows the solar photovoltaic simulator simulating two SPVMs connected in series when the IL is 700 W/m^2, and the temperature is 25 °C. A single SPVM includes 32 SPVCs (8 × 4). Two SPVMs connected in series have 64 SPVCs (8 × 8), 15 of which are shaded. Under this condition, the SPVMs have I_{sc} = 4.7 A, V_{oc} = 90 V, V_{mpp} = 47.2 V, I_{mpp} = 4.25 A, and P_{mpp} = 200.6 W. Figure 17b shows that the solar photovoltaic simulator simulating two SPVMs connected in series when the IL is 65 W/m^2 and temperature = 25 °C. A single SPVM includes 32 SPVCs (8 × 4). Two SPVMs are connected in series, having 64 SPVCs (8 × 8), 30 of which are shaded. Under this condition, the SPVMs have I_{sc} = 0.68 A, V_{oc} = 57 V, V_{mpp} = 17.5 V, I_{mpp} = 0.628 A, and P_{mpp} = 11 W.

Figure 18 displays the $P_{spv}-V_{spv}$ characteristic curve of the SPVM under PSC at IL = 700 W/m^2 and temperature = 25 °C. Figure 18a displays the experimental results of the proposed SLOPDM MPPT control strategy. The angle θ_1 and MPPT duty cycle D were estimated using Equation (8) and Figure 9. The actuating point is accurately operated at MPP P_{mpp} = 200 W. Figure 18b,c are the results of the SAH and the P&O algorithms, respectively. The SAH algorithm's actuating point operated at P_{mpp} = 190 W due to its ability to operate around MPP under PSC. The P&O algorithm's actuating point operated at P_{mpp} = 105 W, which shows that the P&O algorithm is unsuitable under PSC. This is because the actuating point of the P&O algorithm tracks the MPP with the perturbation characteristic, which is suitable to operate on a $P_{spv}-V_{spv}$ characteristic curve with only one MPP (as in the case of UIC). However, $P_{spv}-V_{spv}$ characteristic curve has multiple peak power points under PSC, and the P&O algorithm actuating point will not be able to judge the MPP immediately and produce low power [22].

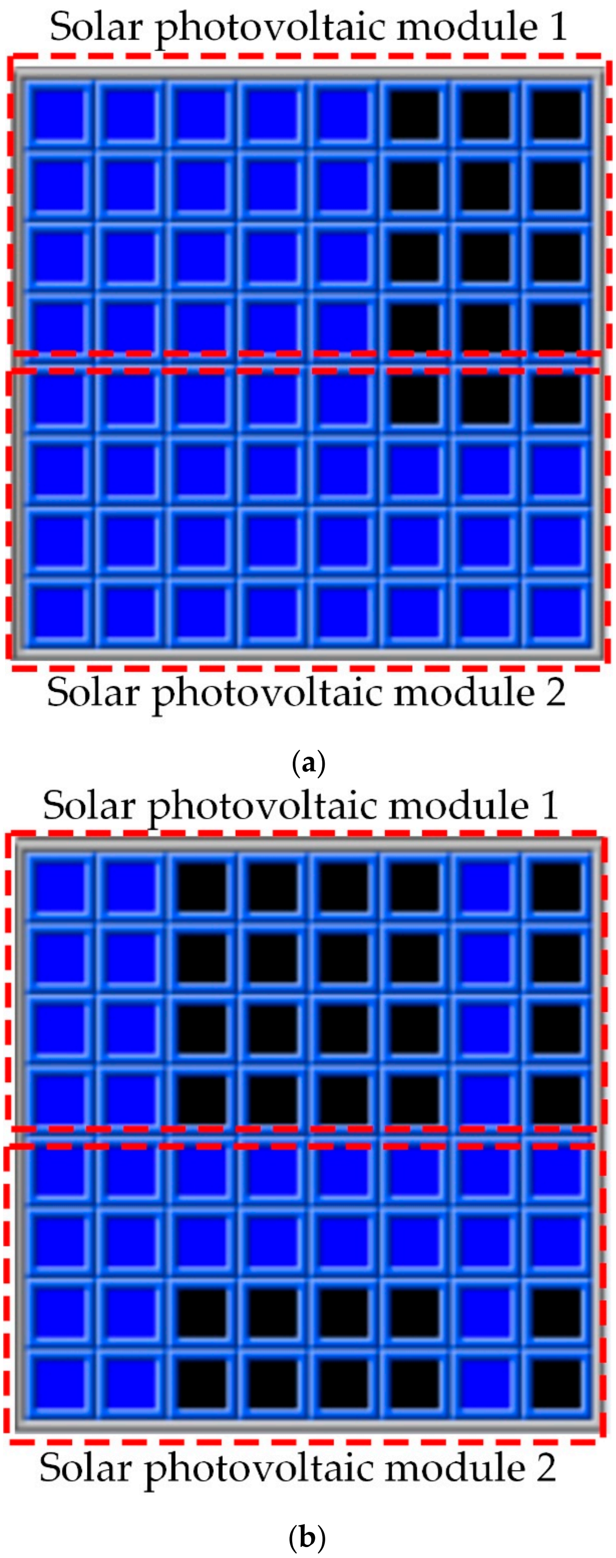

Figure 17. Schematic diagram of the two SPVMs connected in series performing the shadow simulation in the solar photovoltaic simulator at (**a**) IL = 700 W/m^2 and temperature = 25 °C and (**b**) IL = 65 W/m^2 and temperature = 25 °C.

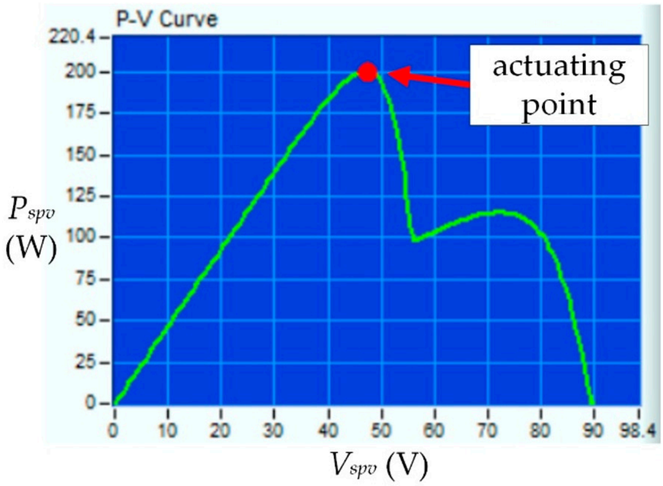

(**a**)

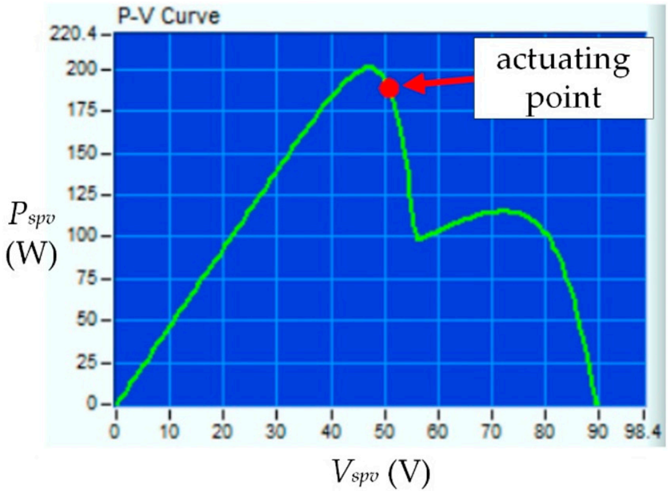

(**b**)

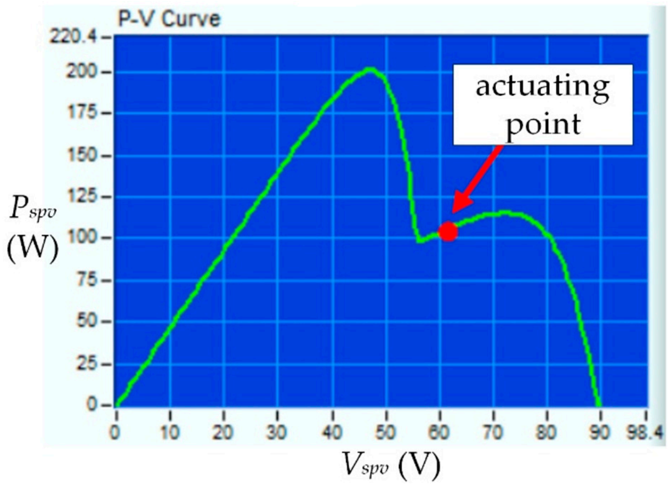

(**c**)

Figure 18. $P_{spv}-V_{spv}$ characteristic curve of SPVM under PSC at IL = 700 W/m^2 and temperature = 25 °C by using the control strategy (**a**) SLOPDM, (**b**) SAH, and (**c**) P&O algorithms.

Figure 19 demonstrate the $P_{spv}-V_{spv}$ curve of the SPVM under PSC at IL = 65 W/m^2 and temperature = 25 °C. Figure 19a displays the experimental results of the proposed SLOPDM MPPT control strategy. First, uses the V_{spv}, I_{spv}, V_o, and I_o measurements. Second, angle θ_1 and MPPT duty cycle D were estimated using Equation (8) and Figure 9. The actuating point is accurately operated at MPP P_{mpp} = 10.9 W like Figure 18a. Figure 19b,c are the results of the SAH and P&O algorithms, respectively. The SAH algorithm's actuating point operated at P_{mpp} = 10.3 W like Figure 18b. The P&O algorithm's actuating point operated at P_{mpp} = 3.9 W like Figure 18c.

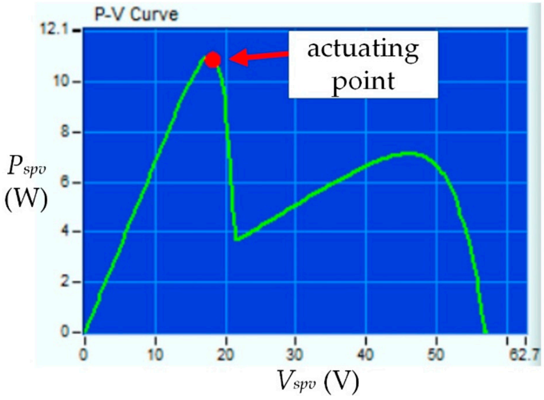

(**a**)

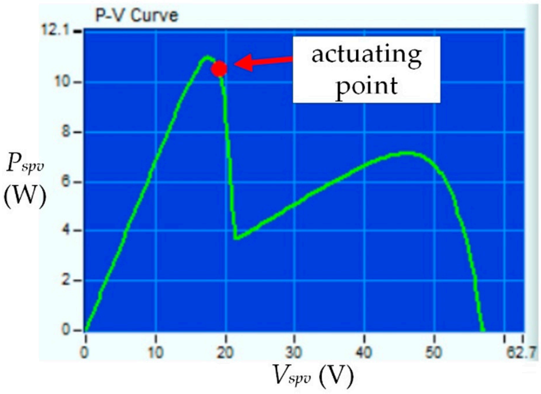

(**b**)

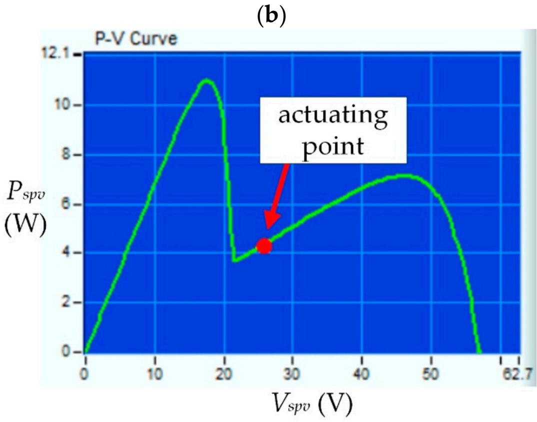

(**c**)

Figure 19. $P_{spv}-V_{spv}$ characteristic curve of SPVM under PSC at IL = 65 W/m^2 and temperature = 25 °C by implementing the control strategy (**a**) SLOPDM, (**b**) SAH, and (**c**) P&O algorithms.

The above results are organized in Table 7, which shows the comparison of proposed SLOPDM, SAH, and P&O algorithms under PSC. The proposed SLOPDM algorithm can reach 99% efficiency under the IL of 700 W/m^2 and 65 W/m^2, whose efficiency is higher than that of the SAH and P&O algorithms.

Table 7. The comparison of proposed SLOPDM, SAH, and P&O algorithms under PSC.

Algorithm	**Efficiency**	
	IL = 700 W/m^2	**IL = 65 W/m^2**
SAH	95%	94%
P&O	52%	35%
SLOPDM	99%	99%

5. Conclusions

This research developed a novel SLOPDM MPPT control strategy for SPPS. The estimation of the optical path angle difference is used as the basis for the proposed control strategy. This is done by determining the relationship between the optical path angle difference, solar photovoltaic power impedance R_{spv} and load R_o, and then calculating the duty cycle corresponding to the MPP, which then drives the boost converter to capture the MPP. The proposed method can easily and rapidly achieve MPP. In this study, the experimental verification is carried out under both the UIC and PSC. The proposed SLOPDM algorithm performance is 99% under UIC, which is higher than that of the SAH and P&O algorithms. In addition, the proposed SLOPDM algorithm reached 99% under PSC with the irradiance level of 700 W/m^2 and 65 W/m^2, while the SAH algorithm efficiencies are 95% and 94%, and the P&O algorithm efficiencies are 52% and 35%, respectively. Under PSC, the proposed SLOPDM algorithm performed far better than the SAH and P&O algorithms. Finally, this novel control strategy does not need to change the hardware circuit design and requires any additional solar power meter. This reduces the cost and the complexity of the system significantly.

Future work can test and verify the proposed SLOPDM MPPT algorithm with multiple sets of SPPS. Furthermore, the related parameters can be modified to make it a faster MPPT control strategy, evaluate the period, and state that SPPS does not have to use MPPT, further improving SPPS efficiency.

Author Contributions: H.-D.L., S.-A.F., S.-D.L., Y.-L.L. and C.-H.L. conceived the presented idea of designing and experiments; H.-D.L. performed testing and verification; H.-D.L., S.-A.F., S.-D.L., Y.-L.L. and C.-H.L. wrote the original draft of this article; H.-D.L., S.-A.F., S.-D.L., Y.-L.L. and C.-H.L. wrote the review and editing of this article; C.-H.L. supervised the findings of this work; all authors provided critical feedback and helped to shape the research, analysis, and manuscript. All authors have read and agreed to the published version of the manuscript.

Funding: This research was funded by the Ministry of Science and Technology, Taiwan, R.O.C., grant number MOST 110-2221-E-011-081 and MOST 110-3116-F-011-002. The authors also sincerely appreciate the considerable support from the Taiwan Building Technology Center from The Featured Areas Research Center Program within the framework of the Higher Education Sprout Project by the Ministry of Education in Taiwan.

Institutional Review Board Statement: Not applicable.

Informed Consent Statement: Not applicable.

Data Availability Statement: Not applicable.

Conflicts of Interest: The authors declare no conflict of interest.

References

1. Pileggi, S.F.; Lamia, S.A. Climate Change TimeLine: An Ontology to Tell the Story so Far. *IEEE Access* **2020**, *8*, 65294–65312. [CrossRef]
2. Akbari-Dibavar, A.; Mohammadi-Ivatloo, B.; Zare, K.; Khalili, T.; Bidram, A. Economic-Emission Dispatch Problem in Power Systems With Carbon Capture Power Plants. *IEEE Trans. Ind. Appl.* **2021**, *57*, 3341–3351. [CrossRef]
3. Andrews, C. Are we geared up for EVs? [EVs-Charging infrastructure]. *Eng. Technol.* **2020**, *15*, 22–25. [CrossRef]
4. Pape, M.; Kazerani, M. Turbine Startup and Shutdown in Wind Farms Featuring Partial Power Processing Converters. *IEEE Open Access J. Power Energy* **2020**, *7*, 254–264. [CrossRef]
5. Jana, A.-S.; Liu, H.-D.; Lu, S.-D.; Lin, C.-H. New Control Scheme for Solar Power Systems under Varying Solar Radiation and Partial Shading Conditions. *Processes* **2021**, *9*, 1359. [CrossRef]
6. Chen, G.; Tang, F.; Shi, H.; Yu, R.; Wang, G.; Ding, L.; Liu, B.; Lu, X. Optimization Strategy of Hydrogovernors for Eliminating Ultralow-Frequency Oscillations in Hydrodominant Power Systems. *IEEE J. Emerg. Sel. Top. Power Electron.* **2017**, *6*, 1086–1094. [CrossRef]
7. Li, H.; Ren, Z. A Tidal Resource Evaluation-Based Method for Tidal Current Generation Farm Allocation Considering the Directionality of Tidal Currents. *IEEE Trans. Sustain. Energy* **2020**, *11*, 2631–2640. [CrossRef]
8. Von Jouanne, A.; Brekken, T.K.A. Ocean and Geothermal Energy Systems. *Proc. IEEE* **2017**, *105*, 2147–2165. [CrossRef]
9. Khaloie, H.; Toubeau, J.-F.; Vallee, F.; Lai, C.S.; Lai, L.L. An Innovative Coalitional Trading Model for a Biomass Power Plant Paired With Green Energy Resources. *IEEE Trans. Sustain. Energy* **2021**, *13*, 892–904. [CrossRef]
10. Leng, K.; Li, S. Distribution Path Optimization for Intelligent Logistics Vehicles of Urban Rail Transportation Using VRP Optimization Model. *IEEE Trans. Intell. Transp. Syst.* **2021**, *23*, 1661–1669. [CrossRef]
11. Park, C.; Lee, S.; Jeong, S.Y.; Cho, G.-H.; Rim, C.T. Uniform Power I-Type Inductive Power Transfer System With DQ-Power Supply Rails for On-Line Electric Vehicles. *IEEE Trans. Power Electron.* **2015**, *30*, 6446–6455. [CrossRef]
12. Farooqui, S.A.; Khan, R.A.; Islam, N.; Ahmed, N. Cuckoo Search Algorithm and Artificial Neural Network-based MPPT: A Comparative Analysis. In Proceedings of the 2021 IEEE 8th Uttar Pradesh Section International Conference on Electrical, Electronics and Computer Engineering (UPCON), Dehradun, India, 11–13 November 2021; pp. 1–5. [CrossRef]
13. Trautz, K.M.; Jenkins, P.P.; Walters, R.J.; Scheiman, D.; Hoheisel, R.; Tatavarti, R.; Chan, R.; Miyamoto, H.; Adams, J.G.J.; Elarde, V.C.; et al. Mobile Solar Power. *IEEE J. Photovolt.* **2012**, *3*, 535–541. [CrossRef]
14. Gong, H.; Rallabandi, V.; Ionel, D.M.; Colliver, D.; Duerr, S.; Ababei, C. Dynamic Modeling and Optimal Design for Net Zero Energy Houses Including Hybrid Electric and Thermal Energy Storage. *IEEE Trans. Ind. Appl.* **2020**, *56*, 4102–4113. [CrossRef]
15. Xu, S.; Shao, R.; Cao, B.; Chang, L. Single-phase grid-connected PV system with golden section search-based MPPT algorithm. *Chin. J. Electr. Eng.* **2021**, *7*, 25–36. [CrossRef]
16. Lu, S.-D.; Wang, M.-H.; Wei, S.-E.; Liu, H.-D.; Wu, C.-C. Photovoltaic Module Fault Detection Based on a Convolutional Neural Network. *Processes* **2021**, *9*, 1635. [CrossRef]
17. Zeng, Q.; Wu, Y.; Wang, B.; Wang, Y.; Wang, R.; Li, J.; Liang, M.; Yang, L.; Xue, S. Unveiling the Role of Conjugate Bridge in Triphenylamine Hole-Transporting Materials for Inverted and Direct Perovskite Solar Cells. *IEEE J. Photovolt.* **2019**, *9*, 1280–1289. [CrossRef]
18. Xu, D.; Zhou, B.; Chan, K.W.; Li, C.; Wu, Q.; Chen, B.; Xia, S. Distributed Multienergy Coordination of Multimicrogrids With Biogas-Solar-Wind Renewables. *IEEE Trans. Ind. Inform.* **2018**, *15*, 3254–3266. [CrossRef]
19. Bollipo, R.B.; Mikkili, S.; Bonthagorla, P.K. Hybrid, optimization, intelligent and classical PV MPPT techniques: A Review. *CSEE J. Power Energy Syst.* **2021**, *7*, 9–33. [CrossRef]
20. Kumar, N.; Singh, B.; Panigrahi, B.K. Integration of Solar PV With Low-Voltage Weak Grid System: Using Maximize-M Kalman Filter and Self-Tuned P&O Algorithm. *IEEE Trans. Ind. Electron.* **2019**, *66*, 9013–9022. [CrossRef]
21. Liu, H.-D.; Lin, C.-H.; Pai, K.-J.; Lin, Y.-L. A novel photovoltaic system control strategies for improving hill climbing algorithm efficiencies in consideration of radian and load effect. *Energy Convers. Manag.* **2018**, *165*, 815–826. [CrossRef]
22. Lu, S.-D.; Lin, C.-H.; Huang, L.-Y.; Lee, Y.-L.; Liu, H.-D.; Liao, P.-C.; Gao, G.-J.; Hsu, C.-M. Novel Global-MPPT Control Strategy Considering the Variation in the Photovoltaic Module Output Power and Loads for Solar Power Systems. *Processes* **2022**, *10*, 367. [CrossRef]
23. Jagadeesan, G.M.; Pitchaimuthu, R.; Sridharan, M. A Two-stage Single-phase Grid-connected Solar-PV System with Simplified Power Regulation. *Chin. J. Electr. Eng.* **2022**, *8*, 81–92. [CrossRef]
24. Uno, M.; Liu, X.; Sato, H.; Saito, Y. Panel-to-Substring PWM Differential Power Processing Converter and Its Maximum Power Point Tracking Technique for Solar Roof of Plug-In Electric Vehicles. *IEEE Access* **2022**, *10*, 42883–42896. [CrossRef]
25. Mobarak, M.H.; Bauman, J. A Fast Parabolic-Assumption Algorithm for Global MPPT of Photovoltaic Systems Under Partial Shading Conditions. *IEEE Trans. Ind. Electron.* **2021**, *69*, 8066–8079. [CrossRef]
26. Zhu, Y.; Wen, H.; Chu, G.; Wang, X.; Peng, Q.; Hu, Y.; Jiang, L. Power-Rating Balance Control and Reliability Enhancement in Mismatched Photovoltaic Differential Power Processing Systems. *IEEE Trans. Power Electron.* **2021**, *37*, 879–895. [CrossRef]
27. Kiran, S.R.; Basha, C.H.H.; Singh, V.P.; Dhanamjayulu, C.; Prusty, B.R.; Khan, B. Reduced Simulative Performance Analysis of Variable Step Size ANN Based MPPT Techniques for Partially Shaded Solar PV Systems. *IEEE Access* **2022**, *10*, 48875–48889. [CrossRef]

28. Hsieh, Y.-C.; Yu, L.-R.; Chang, T.-C.; Liu, W.-C.; Wu, T.-H.; Moo, C.-S. Parameter Identification of One-Diode Dynamic Equivalent Circuit Model for Photovoltaic Panel. *IEEE J. Photovolt.* **2019**, *10*, 219–225. [CrossRef]
29. Pachauri, R.K.; Alhelou, H.H.; Bai, J.; Golshan, M.E.H. Adaptive Switch Matrix for PV Module Connections to Avoid Permanent Cross-Tied Link in PV Array System Under Non-Uniform Irradiations. *IEEE Access* **2021**, *9*, 45978–45992. [CrossRef]
30. Liu, H.-D.; Lu, S.-D.; Lee, Y.-L.; Lin, C.-H. A Novel Photovoltaic Module Quick Regulate MPPT Algorithm for Uniform Irradiation and Partial Shading Conditions. *Processes* **2021**, *9*, 2213. [CrossRef]
31. Park, J.; Jeong, M.-G.; Kang, J.-G.; Yoo, C. Solar Energy-Harvesting Buck–Boost Converter With Battery-Charging and Battery-Assisted Modes. *IEEE Trans. Ind. Electron.* **2020**, *68*, 2163–2172. [CrossRef]
32. Falconar, N.; Beyragh, D.S.; Pahlevani, M. An Adaptive Sensorless Control Technique for a Flyback-Type Solar Tile Microinverter. *IEEE Trans. Power Electron.* **2020**, *35*, 13554–13562. [CrossRef]
33. Nathan, K.S.; Ghosh, S.; Siwakoti, Y.P.; Long, T. A New DC–DC Converter for Photovoltaic Systems: Coupled-Inductors Combined Cuk-SEPIC Converter. *IEEE Trans. Energy Convers.* **2018**, *34*, 191–201. [CrossRef]
34. Lin, M. *Introduction to Solar Cell Technology*; Chuan Hwa Book Co., LTD: Taipei, Taiwan, 2019.
35. Bradley, J. Giving an Account of a New Discovered Motion of the Fix'd Stars. *Phil. Trans.* **1727**, *35*, 637–661. [CrossRef]